Fuel 381 (2025) 133563

Contents lists available at ScienceDirect

Fuel

journal homepage: www.elsevier.com/locate/fuel

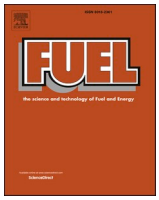

Full Length Article

Analysis of the combustion speed in a spark ignition engine fuelled with hydrogen and gasoline blends at different air fuel ratios

Pedro Gabana [a,*], Blanca Giménez [a], José Martín Herreros [b], Athanasios Tsolakis [b]

[a] Department of Energy and Fluid Mechanics Engineering, University of Valladolid, Paseo del Cauce 59, E-47011 Valladolid, Spain
[b] Department of Mechanical Engineering, University of Birmingham. Edgbaston, Birmingham, B15 2TT, UK

ARTICLE INFO

Keywords:
Hydrogen-Gasoline combustion
Quasi-dimensional combustion diagnosis
Turbulent combustion speed
Premixed combustion
Combustion speed analysis
Expansion speed

ABSTRACT

The use of hydrogen in internal combustion engines is a promising solution for the decarbonisation of the transport sector. The current transition scenario is marked by the unavailability and storage challenges of hydrogen. Dual fuel combustion of hydrogen and gasoline in current spark ignition engines is a feasible solution in the short and medium term as it can improve engine efficiency, reduce pollutant emissions and contribute significantly in tank to wheel decarbonisation without major engine modification. However, new research is needed to understand how the incorporation of hydrogen affects existing engines to effectively implement gasoline-hydrogen dual fuel option. Understanding the impact of hydrogen on the combustion process (e.g. combustion speed) will guide and optimize the operation of engines under dual fuel combustion conditions.

In this work, a commercial gasoline direct injection engine has been modified to operate with gasoline-hydrogen fuels. The experiments have been carried out at various air–fuel ratios ranging from stoichiometric to lean combustion conditions at constant engine speed and torque. At each one of the 14 experimental points, 200-cycle in-cylinder pressure traces were recorded and processed with a quasi-dimensional diagnostic model and a combustion speed analysis was then carried out. It has been understood that hydrogen mainly reduces the duration of the first combustion phase. Hydrogen also enables to increase air excess ratios (lean in fuel combustion) without significantly increasing combustion duration.

Furthermore, a correlation is proposed to predict combustion speed as a function of the fuel and air mixture properties. This correlation can be incorporated to calculate combustion duration in predictive models of engines operating under different fuel mixtures and different geometries of the combustion chamber with pent-roof cylinder head and flat piston head.

1. Introduction

The transport sector is increasingly moving towards decarbonisation. This sector is largely sustained by the use of fossil fuels that are burned in gas turbines or internal combustion engines (*ICEs*) to obtain mechanical energy. Within the transport sector, *ICEs* are the most widespread propulsion systems because they can work in a wide range of operating conditions. On the other hand, the lower the carbon content of fuels, the lower the CO2 emissions in relation to the energy produced in their combustion [1]. As hydrogen has no carbon atoms in its composition, it does not generate CO2 during combustion. Therefore, hydrogen is presented as an alternative to fossil fuels, since its use as a fuel in engines means the reduction of CO2 [2], CO, unburned hydrocarbons and soot emissions [3].

The use of synthetic fuels produced from renewable energy is a way to move away from the use of fossil fuels in *ICEs*. H2 can be produced from renewable electricity with zero CO2 equivalent emissions [3]. Hydrogen in the mobility sector is majorly used in two ways. The first one is the use of hydrogen in fuel cells [3,4]. The second option is the use of hydrogen in thermal engines [3,5]. Within the reciprocating thermal engines, the use of hydrogen in compression ignition engines (*CIE*) has the disadvantage that the autoignition temperature of hydrogen is higher than those of conventional fuels [5]. In spark ignition engines (*SIE*), the use of pure H2 as fuel enables the use of high air–fuel ratios and high levels of residual gas concentrations. The higher the air–fuel ratio or residual gas concentrations, the lower the in-cylinder temperature during the combustion process. The lower the combustion

* Corresponding author.
E-mail addresses: pedro.gabana@uva.es (P. Gabana), blagim@eii.uva.es (B. Giménez), j.herreros@bham.ac.uk (J. Martín Herreros), a.tsolakis@bham.ac.uk (A. Tsolakis).

https://doi.org/10.1016/j.fuel.2024.133563
Received 18 August 2024; Received in revised form 11 October 2024; Accepted 25 October 2024
Available online 3 November 2024

Nomenclature

Variables

A	Area (m^2)
c_l	Turbulence dissipation constant $(-)$
c_p	Specific heat $(J/kg/K)$
c_t	Turbulence production constant $(-)$
D_i	Mass diffusivity of species i in the mixture (kg/m^2)
H_p	Heat power (J/kg)
k	turbulent flux energy (J)
K	Mean flux energy (J)
$k_{\delta l}$	Flame front thickness multiplication term $(-)$
$\mathscr{L}$	Markstein length (m)
L	Length scale (m)
Le_{eff}	Effective Lewis $(-)$
m Mass	(kg)
p	Pressure (Pa)
P	Turbulence production term $(-)$
P_f	Flame front perimeter (m)
$\dot{Q}$	Heat transfer (J/s)
R	Radius (m)
S	Combustion speed (m/s)
T	Temperature (K)
u'	Turbulence intensity (m/s)
V	Volume (m^3)

Acronyms

BMEP	Brake Mean Effective Pressure (bar)
CA	Crank Angle $(^\circ)$
CIE C	ompression Ignition Engine
CoV	Coefficient of Variation
EVC	Exhaust valve closing
EVO	Exhaust valve opening
FSR	Flame speed ratio
G	Gasoline
H2	Hydrogen
ICE	Internal Combustion Engine
IVC	Intake valve closing

Acronyms (cont.)

IVO	Intake valve opening
M	Gasoline hydrogen mixture tests
MFB	Mass fraction burned
NG	Natural Gas
SIE	Spark Ignition Engine
SoI	Start of combustion

Greek letters

α	Angle $(^\circ)$
α_u	Thermal diffusivity unburned products (m^2/s)
β	Zel'dovich number $(-)$
γ	specific heats ratio $(-)$
δ	Flame front thickness (m)
λ	Air fuel equivalence ratio $(-)$
λ_T	Thermal conductivity $(J/(m\,s\,K))$
ρ	Density (kg/m^3)
σ	Density ratio $(-)$
ω	Amplitude growth rate $(-)$

Subscripts

b	Burned
d	Diagnostic
e	Expansion
f	Flame front
i	Integral
k	Kolmogorov
l	Laminar
max	Maximum
p	Piston
pu	Unburned products in contact with the piston
ref	Reference
res	Residual gas concentration
t	Turbulent
u	Unburned
w	Woschni

temperature, the lower the NOx emissions. Performance improvements have also been observed as reported by Kapus et al. [6]. However, the implementation of hydrogen presents several challenges, some of the most important ones are storage and availability [2,7].

The use of dual fuel (hydrogen and gasoline) is presented as a short-term and medium-term alternative to reduce CO2 emissions by unit of energy produced [8,9] without major engine modifications. Previous works have studied how the addition of hydrogen to gasoline affects engine operation [9–11]. Like engines running only with hydrogen, the dual combustion of hydrogen and gasoline in *SIE* allows NOx emissions reductions by operating the engine at higher air–fuel ratio [12]. When hydrogen is added to gasoline, higher combustion speeds are obtained compared to those obtained when the engine operates only with gasoline [13]. It also enables the air–fuel ratio [12] and residual gas concentrations to be increased while maintaining a stable engine operation.

Verhelst et al. [5] pointed out that more studies of hydrogen combustion under engine conditions were required. Until now, the lack of this type of studies is particularly noticeable for the case of hydrogen-gasoline spark ignition engines. The methodology used to study the combustion process characteristics in hydrogen-gasoline blends can be used in the combustion analysis of hydrogen blends with other renewable fuels and under other different engine operating conditions. Going beyond, studying combustion speed permits determine the thermo-fluid-mechanic responsible on how the combustion processes take place unveiling new knowledge to understand the impact of fuels on combustion characteristics.

Applying thermodynamic diagnostic models to in-cylinder pressure traces calculates the amount of energy released in a certain angular timing. The rate at which energy is released is a consequence of the product of the combustion speed and the flame front area. To calculate the combustion speed from heat release rate, it is necessary to use a geometrical model to determine flame front area [14].

The combustion speed calculated with both thermodynamic and geometrical models can be correlated with thermo-fluid-mechanical variables inside the combustion chamber (laminar combustion speed, turbulence intensity, integral length scale, flame front thickness, expansion speed and flame front perimeter).

This knowledge translated into a correlation can be used to predict in-cylinder pressure from the thermo-fluid-mechanical variables in the combustion chamber. For this purpose, the combustion speed obtained with the correlation is used as input to the thermodynamic and geometric models.

This work studies the effects on combustion speed of substituting part of the gasoline fuel with H2 in a commercial spark ignition engine. For this purpose, a blend of gasoline and ethanol is experimentally investigated as the reference/baseline fuel being partially replaced by H2. The in-cylinder pressure records are obtained and processed within a two-zone thermodynamic diagnostic model [14]. The results of the

thermodynamic model are fed into a newly developed geometrical model for pent roof cylinder head combustion chamber which is defined by 6 parameters enabling to adapt the model to cylinder heads with different angle between valves, bores and intersection with the engine head gasket. The outputs of the geometrical model are used to predict combustion speed as a function of the properties of the fuel–air mixtures by using a new methodology, underpinned by Giménez et al. [14] (NG and H2 blends in a Heron piston top combustion chamber). A new methodology for calculating and fitting the correlation of the combustion speed has been proposed. This work demonstrates that the newly proposed correlation can be used to predict the combustion characteristics for different air–fuel ratios and new fuels (e.g. gasoline-hydrogen blends), which could be extended to a variety of spark ignition combustion chamber geometries.

2. Methodology

2.1. Experimental setup

The engine studied is a spark ignition Gasoline Direct Injection Engine. The engine specifications are presented in Table 1.

The original engine has been modified to add H2 in the intake pipe of the engine. The H2 flow rate was measured with a H2 volumetric flow meter (Platon NG series VA GTF-2AHD with a range of 2–44 L/min 1.013 bar 20 °C). Thus, a mixture of air and hydrogen is introduced into the cylinder. The gasoline is supplied directly into the cylinder. Combustion data was measured and logged in one cylinder using an AVL piezo-electric in-cylinder pressure transducer, a charge amplifier (AVL FlexIFEM) and a Baumer (720 pulse per revolution) magnetic crank angle encoder. The pressure data have been recorded each 0.1 crank angle interval using an AVL Indicom system. A schematic diagram of the experimental setup is shown in Fig. 1.

2.2. Experimental methodology

Table 2 shows an overview of the test plan for the engine operating points. Two fuels have been used, gasoline and ethanol E10 (*G*) and the same fuel being replaced by hydrogen at 10 % by mass and 87.3 % by volume (*M*). The fuel–air ratio was also modified from stoichiometric to $\lambda = 1.2$ in *G* and to $\lambda = 2$ in *M*. All experiments have been carried out keeping the engine speed at 2000 rpm and the brake torque at 40 Nm.

The spark timing is set in order to have a mass fraction burned of 50 % (CA50) in a crank angle (CA) of between 3 and 4° after top dead centre as in previous works [12]. At each experimental point, 200 cycles have been recorded and processed.

The fuel flow has been tuned to achieve the target effective torque (40 Nm). By increasing air–fuel equivalence ratio (λ), the intake pressure has been gradually increased to introduce the air or H2/air mixture (depending on the case) required to achieve the λ value specified. Consequently, the maximum engine pressure is increased. The amount of energy introduced into the engine per cycle is similar in all experimental points. As λ increases, less fuel is introduced, this is because the indicated efficiency increases with λ.

Table 1
Engine geometric specifications.

Bore x Stroke	84 x 90 mm
Number of cylinders	3
Number of Valves	12
Displacement	1497 cm^3
Compression Ratio	11:1
IVO	20 CAD
IVC	−88 CAD
EVO	92 CAD
EVC	0 CAD
Inlet valve peak lift	10 mm
Exhaust valve peak lift	9 mm
Total Crank/Piston offset	9.6 mm

2.3. Data processing

The methodology followed during the diagnostic process is summarised in the following steps:

1. Data filtering using an adaptive filter based on Savitzky-Golay polynomials [15] to obtain a continuous and derivable pressure signal at each cycle.
2. Determination of pressure and angle offsets, compression ratio (10.8) and heat transfer coefficient (0.9). For this, a methodology based on genetic algorithms is used, as stated by Reyes et al. [16]. Except for the pressure offset, which is chosen for each cycle, the rest of the variables take the same value in all experimental conditions.
3. Processing of the filtered pressure data with a two-zone diagnostic thermodynamic model [14,17]. The thermodynamic diagnostic model allows calculating the burned mass rate, dm_b/dt, from dp/dt obtained processing pressure data. More information about the thermodynamic model is available in Mendeley data section.
4. Processing of the resulting data of burned products volume with a geometric model that enables calculating flame front radius (R_f) and flame front area (A_f). The flame front area is combined with dm_b/dt to calculate the combustion speed (S_d) Eq. *(1)*.

$$\frac{dm_b}{dt} = S_d A_f \rho_u \tag{1}$$

5. Average combustion speed calculation for each flame front position in a population of 200 cycles. A cycle averaged combustion speed result is obtained for each test point and flame front position inside the combustion chamber. The results are independent of the crank angle at which they take place and dependent on the position in the combustion chamber.

3. Geometric model

Based on the volume of mass burned, which is the result of the thermodynamic model, the idea is to determine the radius of the sphere centred on the spark plug intersecting with combustion chamber walls and the flat piston. The combustion chamber is defined by the 6 parameters. Once the radius of the sphere has been determined, the next objective of the model is to calculate the area of the sphere contained in the combustion chamber. This area is the one used in Eq. *(1)*. For this purpose, the combustion chamber in the cylinder head is assumed to be delimited by (Fig. 2):

- Two inclined and symmetric planes forming the angle α_t, the intersection horizontal line of the two planes is located at a distance Z_v from the spark plug.
- A half-angle cone α_C with a base at the cylinder head gasket having a diameter equal to the Bore.
- Two vertical planes at a distance Y_p from the cylinder axis.
- A horizontal plane at a distance Z_t over the spark plug.
- The plane of the cylinder head gasket is at a distance Z_c from the spark plug.

The combustion chamber volume below the cylinder head gasket is delimited by:

- Cylinder head gasket plane.
- The cylinder of diameter 2 R_p.
- The piston plane located at a distance X_p from the cylinder head gasket.

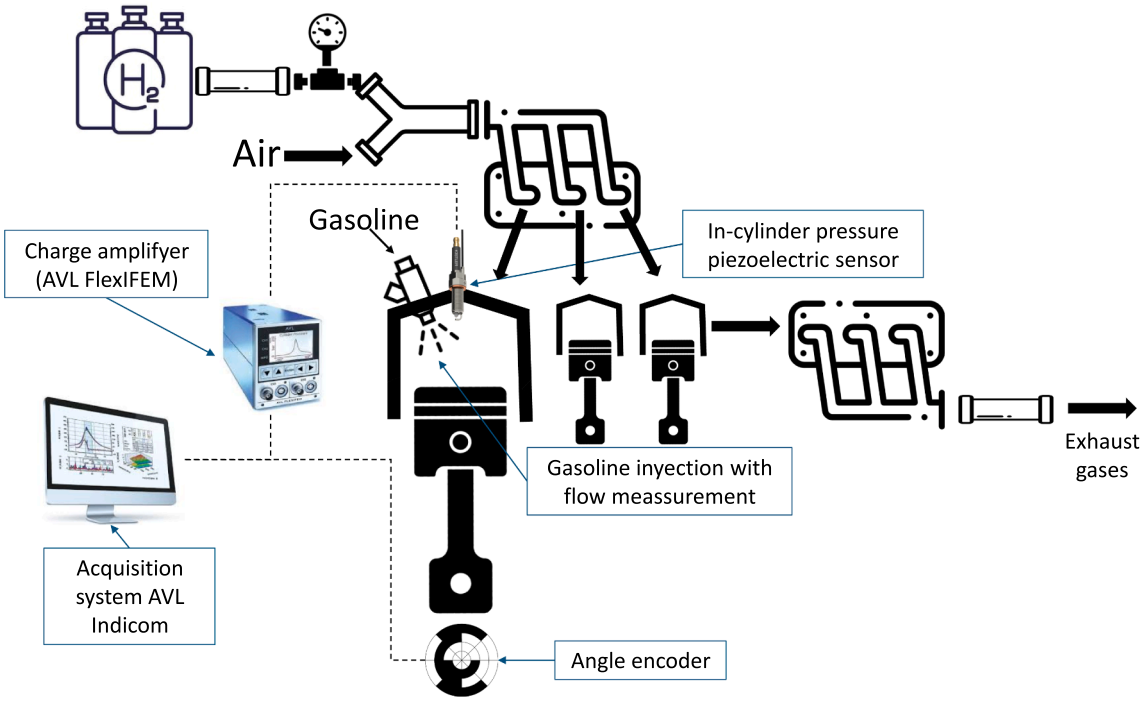

Fig. 1. Experimental facility schematic diagram.

Table 2
Characteristics of the 14 test points analysed at Me = 40Nm, n = 2000 rpm, BMEP = 3.35 bar.

Name	λ	$\dot{m}_f$(kg/h)	$\dot{m}_a$(kg/h)	SoI (°CA)	p_{IVC}(bar)	p_{max}(bar)	Indicated efficiency (%)	Y_{res}(%mass)
G 1	1.0	0.785	11.614	−32.4	1.01	29.51	34.9	19.9
G 1.1	1.1	0.760	12.369	−35.9	0.95	29.49	36.4	18.9
G 1.2	1.2	0.760	13.481	−41.2	1.01	29.87	36.5	18.4
M 1	1.0	0.638	10.833	−20.3	1.02	28.87	34.9	21.7
M 1.1	1.1	0.657	12.283	−21.1	1.11	30.09	35.8	20.7
M 1.2	1.2	0.634	12.942	−21.7	1.12	30.04	36.9	21.2
M 1.3	1.3	0.623	13.784	−23.6	1.17	30.67	37.7	21.2
M 1.4	1.4	0.612	14.580	−25.2	1.21	30.90	38.5	21.2
M 1.5	1.5	0.602	15.389	−26.5	1.24	31.57	39.2	21.2
M 1.6	1.6	0.610	16.605	−28.5	1.28	32.00	39.7	21.2
M 1.7	1.7	0.593	17.172	−28.5	1.30	31.66	40.2	21.2
M 1.8	1.8	0.588	18.040	−33.1	1.37	33.18	40.5	21.1
M 1.9	1.9	0.585	18.945	−36.2	1.40	33.30	40.7	20.7
M 2	2.0	0.586	19.984	−41.4	1.45	34.54	41.1	20.6

The volume covered by the sphere of radius R_f is calculated from horizontal planes at different distances Z from the spark plug. The intersections of these planes with the combustion chamber result in a geometry of stadiums defined by two parallel lines and a circle centred on the spark plug. The intersection of the plane with the sphere volume has the same geometry unless the sphere does not intersect in that plane with the cylinder head, then it is a circle. The burned products volume outside the cylinder head corresponds to the intersection of a sphere of radius R_f with the plane of the piston and cylinder. Full geometric model description is available in Mendeley data section.

In Fig. 2 two side views with the parameters characterizing the model are shown. The floor plane shows a horizontal plane located at a distance Z from the spark plug.

Fig. 3 shows an image of the burned volume at a certain piston position and for a certain flame front radius. Fig. 3 has been obtained with Autodesk Inventor software. This software has been used to validate the geometric model.

4. Combustion properties

4.1. Until this section, the methodology for processing the experimental data to calculate the combustion speed (S_d) has been presented. These results and their analysis are presented in section 5.1. The final objective of this work, as mentioned in the introduction, is to predict combustion speeds (S_t) from the thermo-fluid-mechanical variables inside the combustion chamber. This section explains how to calculate the variables (laminar combustion speed, residual exhaust gases concentration, turbulence intensity and flame properties) dependent on the conditions in the combustion chamber necessary to fit the correlation of the combustion speed (S_t) in section 5.2.Laminar combustion speed

Hydrogen-gasoline mixtures laminar combustion speed (S_l) determination has been previously addressed in the literature [18,19]. The laminar combustion speed depends on the pressure and temperature conditions and on the mixture composition, determined by the proportion of hydrogen in the fuel, the air excess ratio (λ) and mass fraction of combustion products Y_{res}. The expression proposed by [19] has been used as Eq. (2), which is valid for the engine operating conditions.

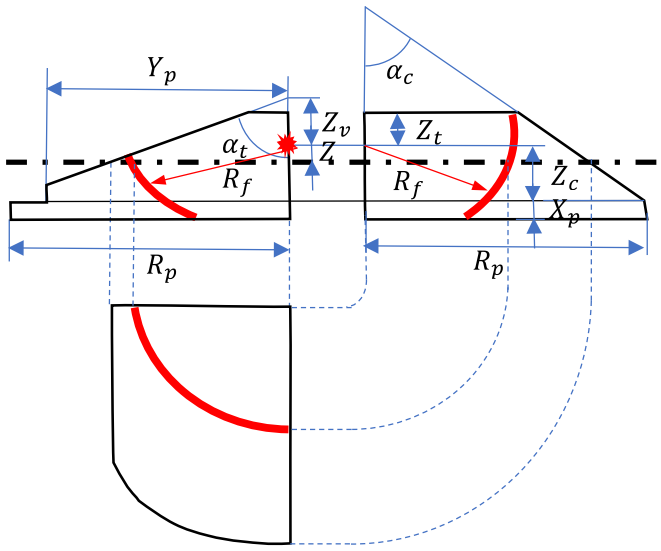

Fig. 2. 1/4 cylinder head views with one of the section planes used to calculate the intersection of the burned volume with the cylinder head.

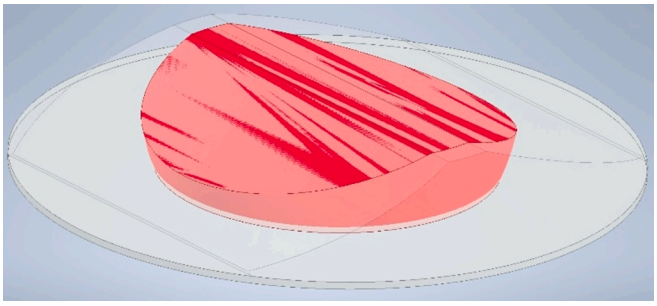

Fig. 3. Autodesk Inventor representation showing the interaction of the flame front with the combustion chamber walls.

$$S_l = S_{l0}\left(\frac{T_u}{T_{ref}}\right)^{\alpha_T}\left(\frac{p}{p_{ref}}\right)^{\beta_p}(1-2.1Y_{res}) \tag{2}$$

Where T_u (K) is the unburned products temperature, p (bar) is the pressure, and the reference temperature and pressure are respectively 298 K and 1 bar. S_{l0}, α_T and β_p can be calculated according to the expression proposed in [19]. These three parameters depend on the hydrogen volume fraction in the intake gas and λ.

Eq. *(2)* provides laminar combustion speed (S_l) dependent on the combustion chamber conditions.

Experiments at low pressures and temperatures show that the combustion speeds of ethanol and *iso*-octane are similar [20]. Simulations for the calculation of the laminar combustion speed of gasoline-ethanol blends at high pressures and temperatures show that the presence of ethanol in gasoline has little influence on the laminar combustion speed compared to pressure, temperature, fuel air ratio and recirculated exhaust gases [21]. For this reason, the laminar combustion speed has been considered to be similar to a mixture of *iso*-octane and hydrogen; however, the flame properties in section 4.4 have been calculated considering the composition of the mixture.

4.2. Residual exhaust gases

The residual gases mass fractions were calculated by simulating the gas exchange process with AVL BOOST software. The same distribution diagram as in the real engine has been considered and the intake pressure has been set to obtain the same average mass flow rate as the measured mass flow rate at each test point. The results are shown in Table 2.

4.3. Turbulence intensity

Turbulence intensity (u') is calculated using the simplified K-k model [22] applied to a closed system. This model has as initial conditions at intake valve closing time an average kinetic energy of the mixture K_{IVC} and a turbulent kinetic energy k_{ICV} dependent on u'. Energies evolve according to the equations of the model Eq. *(3)*.

$$\frac{dK}{dt} = -P + K\frac{\dot{\rho}_u}{\rho_u}$$

$$\frac{dk}{dt} = P - m\varepsilon + k\frac{\dot{\rho}_u}{\rho_u}$$

$$k = \frac{3}{2}mu'^2P = 0.3307c_t\sqrt{\frac{3}{2}}\frac{K}{c_l\frac{V}{A_p}}u'\varepsilon = \frac{u'^3}{c_l\frac{V}{A_p}} \tag{3}$$

Where P is the turbulent kinetic energy production term from the average kinetic energy of the mixture, ε is the turbulent kinetic energy dissipation term, V is the combustion chamber volume and A_p is the piston area. Initial kinetic energies K_{IVC} and k_{ICV} have been chosen to match those obtained with the gas exchange model developed in AVL BOOST at the instant of intake valve closing.

The model has two tuning parameters, $c_t = 0.6$ which is a constant affecting turbulence production and $c_l = 0.3$ affecting turbulence dissipation. Both parameters have been tuned following the AVL BOOST guidelines so that u' at top dead centre has values between one and two times the mean linear piston speed.

4.4. Flame properties

4.4.1. Laminar flame front thickness

The laminar flame front thickness (δ_l) is defined using the diffusion scaling approach.

$\delta_l = \alpha_u/S_l$ as in [23,24]. The thermal diffusivity of the mixture (α_u) is defined as $\alpha_u = \lambda_T/(\rho_u c_p)$ [25]. The procedure proposed by Mathur et al. [26] is followed to calculate the thermal conductivity of the mixture λ_T. The c_p of the mixture has been calculated following a molar fraction weighted formulation by calculating the c_p of each species with the correlations of NIST [27].

4.4.2. Effect of instabilities on flame front thickness

Instabilities cause an increase in flame front thickness which is quantified by the parameter $k_{\delta l}$ introduced in [14] Eq. *(4)*.

$$k_{\delta l} = \exp\left(2\pi\omega_{DL} - \mathscr{L}\frac{\sigma(1+\omega_{DL})(\sigma+\omega_{DL})}{\sigma+(\sigma+1)\omega_{DL}}\frac{4\pi^2}{L_I}\right) \tag{4}$$

This term includes hydrodynamic and thermo-diffusive instabilities. The term ω_{DL} is only dependent on the density ratio σ. Furthermore, $\mathscr{L}$ is the Markstein number, which depends on the effective Lewis, Zel'dovich number and σ [28] Eq. *(5)*.

$$\mathscr{L} = \delta_l\left[\frac{\sigma ln\sigma}{\sigma-1} + \frac{\beta(Le_{eff}-1)}{2(\sigma-1)}\int_1^{\sigma}\frac{lnx}{x-1}dx\right] \tag{5}$$

4.4.3. Zel'dovich number

Zel'dovich number is defined as $\beta = (E_a(T_b^0 - T_u))/(RT_b^{0^2})$. Where T_b^0 is the adiabatic flame temperature and E_a is the activation energy. The activation energy can be calculated according to Eq. *(6)* [29].

$$E_a = -2R\left[\frac{\partial ln(\rho_u S_l)}{\partial\left(\frac{1}{T_b^0}\right)}\right]_p \quad (6)$$

4.4.4. Effective Lewis

Effective Lewis is defined as $Le_{eff} = \alpha_u / D_i$. The mass diffusivity ($D_i$) is a property of a species in the mixture calculated with the Blanc's law presented in [25]. In this work binary mass diffusivities have been calculated according to [25].

However, when there are mixtures of various fuels, there are different methodologies to calculate Le_{eff}. In [23] various methodologies for the calculation of the effective Lewis of several hydrocarbon and hydrogen mixtures are analysed. The effective Lewis have been calculated according to the heat release-based approach Eq. (7) using the results obtained in [23] and the hydrogen concentrations in the experimental data set of this work.

$$Le_{eff} = 1 + \frac{q_1(Le_1 - 1) + q_2(Le_2 - 1)}{q_1 + q_2} \quad (7)$$

Where q_1 and q_2 correspond to the energy released by each fuel in the mixture and Le_1 and Le_2 are the Lewis numbers of each fuel species.

5. Results

5.1. Thermodynamic diagnostic model results

From the pressure signal, mass fraction burned (*MFB*) is calculated. From *MFB*, CA timings can be calculated. Fig. 4 (a) shows the average CA timing from the start of combustion to $MFB = 0.1$ and from $MFB = 0.1$ to $MFB = 0.9$. CA timings are calculated from mass fraction burned (*MFB*) and pressure signal. CA0-90, CA0-10 and CA10-90 are considered to quantify the duration of the total combustion process, the first phase of combustion and the main or second phase of combustion, respectively. The addition of hydrogen clearly decreases the duration of the combustion process for the same air to fuel ratio (Fig. 4 (a)). In *G*, the first phase of combustion has a longer duration than the second phase. In *M* the opposite occurs (CA10-90 < CA0-10) for all λ values lower than 1.9. For both cases (G and M), when λ increases, the share of the first phase of combustion with respect to the total combustion time increases, in agreement with the results of [30,31]. When comparing the results of *G* with *M* for λ values between 1 and 1.2, it is concluded that the addition of hydrogen to the fuel leads to a reduction in the first phase of combustion (CA0-10) of between 40 % (λ = 1) and 50 % (λ = 1.2). However, for the second phase of combustion the reduction ranged from 8 % (λ = 1) to 16 % (λ = 1.2). Therefore, the addition of hydrogen overall reduced the combustion duration but affecting more to the first phase than the second phase of combustion.

CA0-10 is divided into CA0-1 and CA1-10, Fig. 4 (b). CA0-1 includes the growth of the flame kernel and the transition to turbulent regime [32]. CA0-1 is larger than CA1-10 for all experiments. Both CA0-1 and CA1-10 increased with λ for G and M fuels, but CA0-1 increased much more than CA1-10. Therefore, most of the increase in CA0-10 with increasing λ is due to the increase in CA0-1.

Fig. 5 (a) shows S_d values versus R_f for 200 cycles of the *G*1.1 experiments. Comparing the S_d results for each cycle for the same flame radius enables to analyse the cycle-to-cycle fluctuations and to determine the averaged combustion speed when the flame front passes through a certain position. Fig. 5 (b) shows the coefficient of variation (*CoV*) as a function of flame front radius. The dispersion for all radii between 10 and 40 mm is between 9 % and 14 %. It should be noted that all the experiments have been carried out with the engine running at the same engine speed and, therefore, the turbulence levels are very similar for all experiments.

Fig. 6 (a) shows R_f as a function of *MFB* averaged for all experimental conditions. The mean *MFB* value is also plotted and highlighted, obtaining very similar values for all experimental conditions. Fig. 6 (b) shows the cycle averaged combustion speed (S_d) at the same flame front position (same R_f) for 200 cycles at the 14 experimental conditions. On the bottom horizontal axis an approximate value of the mass fraction burned (*MFB*) is presented.

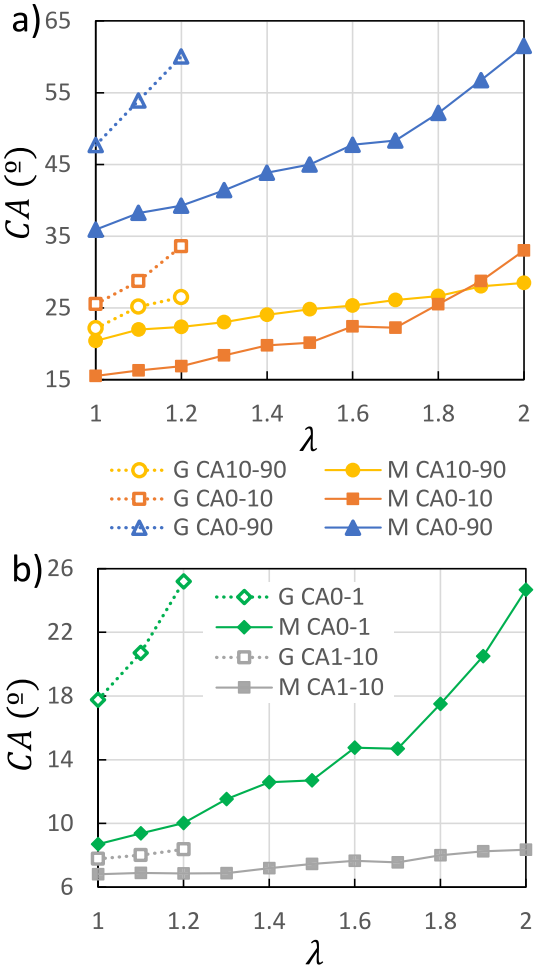

Fig. 4. (a) Duration of the first phase of combustion (CA0-10), the second phase of combustion (CA10-90) and the total combustion duration (CA0-90) as a function of λ for *M* and *G* experiments. (b) Values of CA0-1 and CA1-10 as a function of λ for *M* and *G* experiments.

The values for flame front radii $R_f < 10$ mm correspond to $MFB < 1\%$. The combustion speed values in this zone (Fig. 6 (b)) are not reliable because there is not enough resolution in the pressure signal derivative. Thus, it is not possible to obtain reliable information about the kernel growth. Therefore, the results of Fig. 6 (b) are analysed in more detail for flame front positions larger than 10 mm where MFB > 1 %.

In the R_f range from 10 mm to 20 mm (CA1-10 approximately) the S_d of *G* are lower than those of *M*. A large influence of λ on S_d for λ values between 1 and 1.2 is not obtained in either of the two fuels. In *M* when the value of λ exceeds 1.2, in the R_f range between 15 and 20 mm, the influence of λ is slightly appreciated, so that S_d decreases when λ increases. These trends are shown in CA1-10 (Fig. 4 (b)). CA1-10 values do not significantly vary with λ, being *G* values larger than those obtained for *M*. Increasing λ in *M* experiments slightly increases CA1-10. This combustion phase takes place in an angular interval between 6 and 9 crank angle degrees.

In the second phase of combustion quantified by CA10-90 (approximately $R_f > 20$ mm and $R_f < 40$ mm), the influence of λ on S_d for both

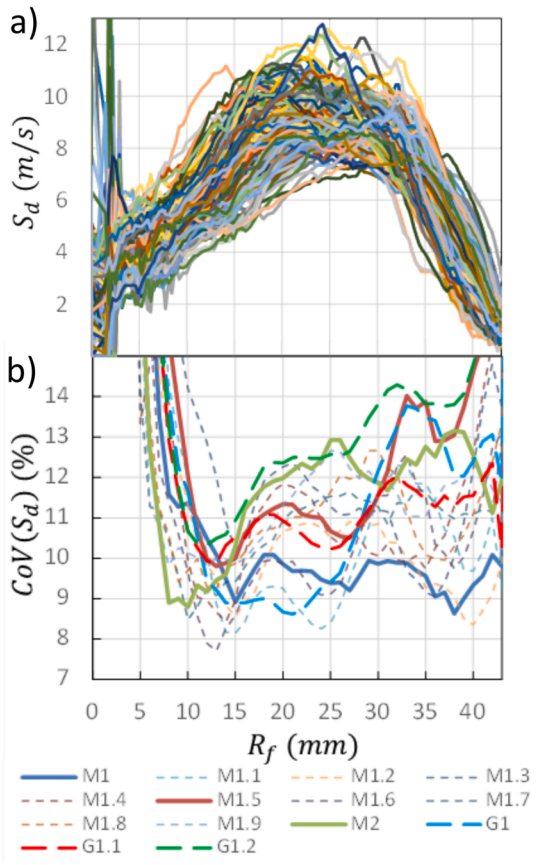

Fig. 5. (a) S_d as a function of R_f for all cycles of $G1.1$. (b) Coefficients of variation of S_d as a function of R_f for all experimental points.

M and G is observed. In this second phase, combustion speeds of G cease to be lower than those of M. S_d trends are reflected in the CA10-90 values in Fig. 4 (a), the higher the S_d the lower the CA10-90 values.

As combustion evolves, S_d values for G grow faster than those of M results. The point at which the flame front reaches the piston, approximately $R_f = 14$ mm, is also observed. This point is very similar for all the experiments, since the combustion process takes place at crank angle times when the piston is close to top dead centre.

Fig. 6 (c) shows S_l cycle averaged at each experiment as a function of R_f. Each S_l has been calculated with Eq. *(2)* as a function of the thermodynamic conditions of the mixture at each instant. S_l values increase with decreasing λ. The addition of hydrogen makes S_l values with M larger than with G for the same λ values. The difference that exists between S_l values are weakly reflected in S_d in the first phase of combustion $R_f < 20mm$. In the second phase, S_l values are ordered with λ, the higher λ the lower S_l. At $R_f = 30mm$ an increase in S_l around 550 % is reflected in an increase around 30 % in S_d. Turbulence influence increases strongly with decreasing S_l.

The Flame Speed Ratio is defined as $FSR = S_d/S_l$. Fig. 6 (d) shows $ln(FSR-1)$ cycle averaged as a function of R_f for all experiments. It is observed that FSR depends on R_f but more on λ. The FSR trend is explained by the fact that S_l varies largely with λ while S_d takes values in the same order for all λ values. According to Gülder [33], FSR is primarily dependent on the ratio u'/S_l. The u' value is very similar at all experiments since the engine speed is the same. Therefore, the variation of FSR between all experiments is due to the variation of S_l.

S_d values for different R_f are shown as a function of λ, Fig. 7. For λ values lower than 1.2 and $R_f \leq 20mm$ in both G and M there is no clear trend with λ. For higher R_f values, the trend of S_d when increasing λ is as expected from the trend of S_l. In the case of M with $\lambda > 1.2$ the trends are

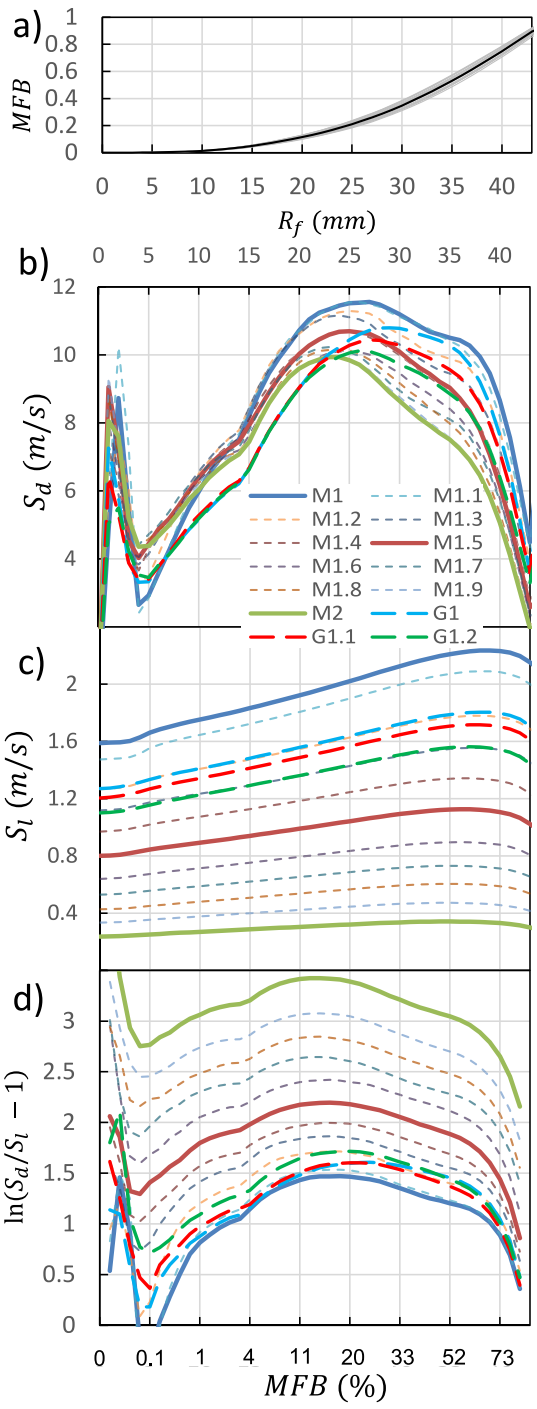

Fig. 6. (a)*MFB* cycle averaged as a function of R_f and in thicker line the average of all experimental conditions. (b) S_d cycle averaged as a function of R_f. (c) S_l cycle averaged as a function of R_f. (d) FSR for all experiments cycle averaged as a function of R_f.

decreasing with λ at all R_f values. The trend of decreasing S_d with increasing λ is larger as R_f increases.

5.2. Prediction of flame speed ratio (FSR)

Gülder [33] proposed a relationship between the turbulent (S_t) and the laminar combustion speed (S_l) depending on u'/S_l and L_i/δ_l [28]. This relationship describes the free-field combustion behaviour, Eq. *(8)*.

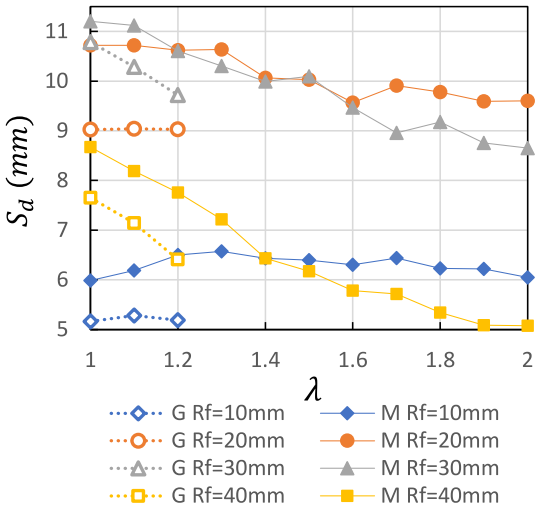

Fig. 7. S_d as a function of λ for different R_f.

$$\frac{S_t}{S_l} - 1 = k_0 \left(\frac{u'}{S_l}\right)^a \left(\frac{L_i}{\delta_l}\right)^b \tag{8}$$

For the case of internal combustion engines, Giménez et al. [14] proposed a new correlation which considers the effect of instabilities increasing the apparent thickness of the flame front (δ_l) through a laminar flame front thickness multiplier $k_{\delta l}$. Giménez et al. [14] also added a new term to quantify that the flow is confined by the walls of the *ICE* combustion chamber (confined combustion). It was suggested that having a confined combustion produces an additional turbulence that is taken into account with a new term called as the entrainment velocity (S_e), defined as the speed of the reactants close to the flame front. This speed, close to the walls, produces shear stresses that cause further turbulence. The amount of turbulence that is generated and affects the combustion speed depends on the length of the intersection between the flame front and the combustion chamber walls. In this work it is referred to as the flame front perimeter P_f. Considering S_e the intensity of the new turbulence generated, the new correlation term includes the relation between the expansion speed S_e and the laminar combustion speed S_l and also the influence of the perimeter of the flame front non-dimensionalised with the integral scale L_i Eq. *(9)*.

$$\frac{S_t}{S_l} - 1 = a \left(\frac{u'}{S_l}\right)^b \left(\frac{L_i}{\delta_l k_{\delta l}}\right)^c \left(\frac{S_e P_f}{S_l L_i}\right)^d \tag{9}$$

According to Giménez et al. [14] if mean properties over the whole combustion chamber are considered, S_e can be calculated with Eq. *(10)*.

$$S_e = \frac{1}{A_f}\left[\frac{dV}{dt}\left(\frac{A_{pu}}{A_p} - \frac{V_u}{V}\right) + V_u \dot{m}_{bb}\right] + S_t\left(\frac{(\gamma-1) m_u H_p}{\gamma p V}\right) + \frac{(\gamma-1)}{\gamma p A_f}\left(\dot{Q}_w \frac{V_u}{V} - \dot{Q}_u\right) \tag{10}$$

The correlation proposed by Giménez et al. [14] has the drawback that S_e depends on S_t so it is not an explicit expression. In this work, an iterative new method to calculate S_t is used. The method consists of making a hypothesis of S_t and substituting it in Eq. *(10)* to calculate S_e and then the new S_t with Eq. *(9)*. The process is repeated iteratively until both S_t values match. In [14] the coefficients were fitted using multilinear regressions. However, the current methodology does not allow to fit the coefficient a and the exponents b, c and d to the experimental data using the method proposed in [14]. In this work, the coefficients have been fitted using a new optimisation method. The method is based on using a genetic algorithm integrated in Matlab in which the function to be optimised is the mean square error between S_d and the predicted combustion speed S_t. For 12 specific values of the flame front radius between 10 and 37 mm, the average values of all variables involved in the correlation have been calculated over 200 cycles, resulting in 12 different values of all variables at the 14 experimental conditions. The results from the fit are shown in Fig. 8.

Table 3 shows the correlation coefficients obtained in [14], the coefficients obtained in this work and the coefficients of the fit of the data from [14] using the methodology of this work.

The exponents of the correlation obtained following the new methodology proposed in this work, where S_e depends on S_t, are very similar for the two data sets (cases 2 and 3). There is a remarkable difference, especially in the exponent of the third term, d, when it is calculated with the experimental values of S_d (cases 1 and 3). The third term is calculated with S_t and it is the term modified in the iterative process.

The estimation of u' greatly affects the coefficient a of Eq. *(9)*. The value of a obtained in case 2 is lower than in case 3. In this work the values of u' at top dead centre divided by the piston mean linear velocity are larger than in [14]. An underestimation of u' in [14] or an overestimation in this work would justify the differences in the value of a. Even with very different combustion chamber geometries (pent-roof cylinder head vs flat cylinder head) the correlation exponents take very similar values in cases 2 and 3.

Fig. 9 shows the Borghi-Peters diagram [34,35] and the location of the experimental conditions for four flame front positions (15, 22, 30 and 37 mm), under two laminar flame front thickness hypothesis δ_l and $\delta_l k_{\delta l}$.

Three iso-*FSR* lines have been added ($FSR = 2$, $FSR = 10$ and $FSR = 30$) into Fig. 9. These iso-*FSR* lines have been calculated by using the expression of Gülder [33] corresponding to free field combustion.

Considering δ_l as the flame front thickness, when λ increases, as S_l decreases and u' has similar values, the points move from the zone with $L_k > \delta_l$ to the zone $L_k < \delta_l$ by changing the combustion regime. Therefore, if it is assumed that the flame front thickness is increased by the instability (flame front thickness as $\delta_l k_{\delta l}$) the combustion regime in all experimental conditions is in the thin reaction zone instead of close to

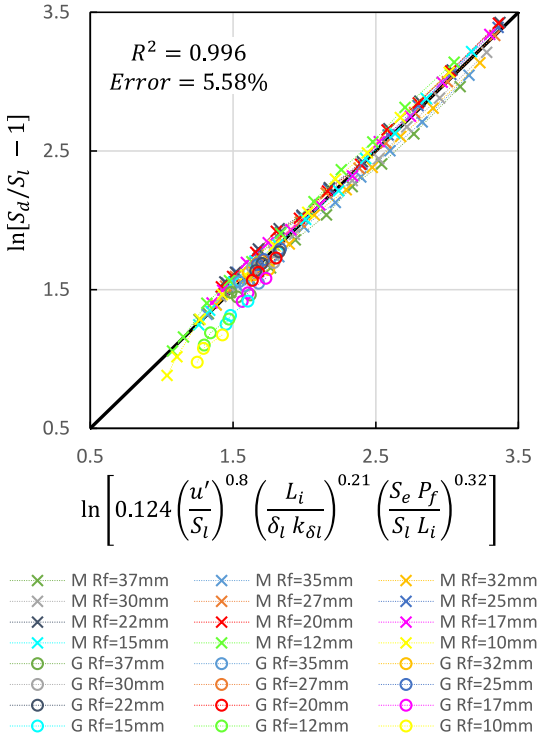

Fig. 8. Experimental data of ln(Sd /Sl − 1) versus values obtained from the correlation. The plot includes12 flame front positions for *M* and *G*.

Table 3
Fitting results with different data and methodology.

Case	Data	Methodology	a	b	c	d
1	[14]	[14]	0.114	0.86	0.29	0.4
2	This work	This work	0.124	0.8	0.21	0.32
3	[14]	This work	0.21	0.85	0.26	0.31

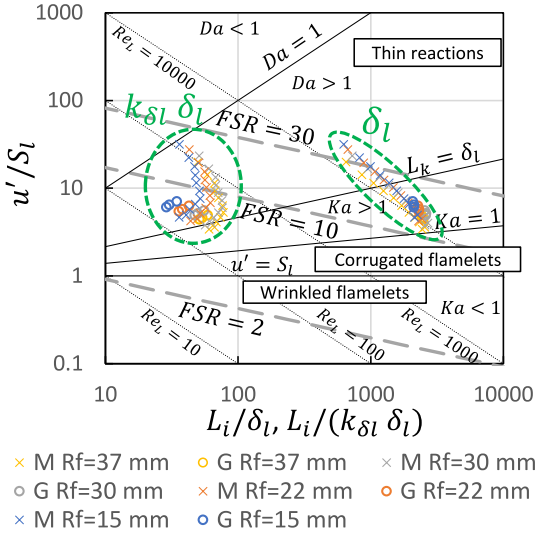

Fig. 9. Borghi-Peters diagram and experimental results for 4 flame front positions. The efect of considering the flame front thickness as δ_l (points on the right) and as δ_l $k_{\delta l}$ (points on the left) is shown.

the corrugated flames zone.

It is observed that the test points would be located approximately between $FSR = 10$ and $FSR = 30$ [33] when the flame front thickness is δ_l. If the influence of instabilities in the flame front thickness ($\delta_l k_{\delta l}$) is taken into account, the points are shifted to the left with lower *FSR* values.

5.3. Understanding the effect of the correlation terms on FSR prediction

First and third terms of Eq. (9) quantify the relationship between the turbulence intensity in the combustion chamber and the laminar combustion speed. The turbulence intensity can be caused by the fluid velocity in the combustion chamber or by the expansion of the reacting gases. The second term reflects the influence of the ratio of the characteristic turbulence dimension L_i to the flame front thickness modified by instabilities.

Fig. 10 shows the three combustion terms as a function of the flame front radius for all experimental conditions. The trend of u'/S_l with R_f is shown in figure Fig. 10 (a). The trend is always decreasing as R_f increases since the turbulence intensity decreases with time due to its dissipation and S_l increases due to temperature increase. In Fig. 10 (c) the trend of the term $(S_e P_f)/(S_l L_i)$ with R_f is shown. This term is the one that provides the shape of S_t as a function of R_f. As mentioned above, this term is attributed to the turbulence generated by the unburned gas speed with respect to the combustion chamber walls. The trend with respect to λ is the same as u'/S_l, mainly due to the decrease of S_l.

In first and third terms of Eq. (9), the representative curves of each λ do not intersect when changing R_f, so they can hardly explain the different trend when varying the radius of *G* and *M* Fig. 4 (a). Fig. 10 (b) shows that $L_i/(\delta_l k_{\delta l})$ term does not maintain the same trend against R_f for all λ values. The value of this term is not ordered as a function of λ for a fixed R_f as in the other two correlation terms. For the same R_f value, the highest values of this term are reached at λ values of about 1.5 in *M*.

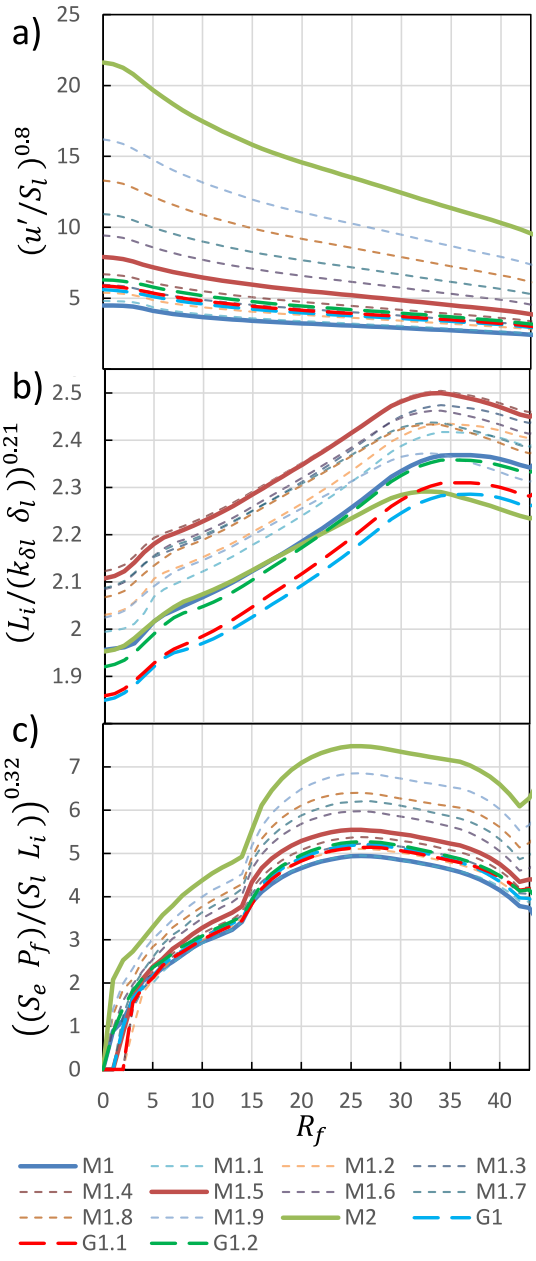

Fig. 10. Cycle averaged values of the correlation terms Eq. (9) as a function of R_f for all experimental conditions. (a) u'/S_l. (b) $L_i/(\delta_l k_{\delta l})$. (c) $(S_e P_f)/(S_l L_i)$.

The term takes similar values for $\lambda = 1$ and for $\lambda = 2$ in *M* for R_f values lower than 20 mm. Subsequently, at values of $R_f > 20mm$ the term takes larger values in *M*1 than in *M*2. *G* values have trends with R_f similar to those in *M*1, but with smaller values. In *M* results, the higher the λ, the higher the value of the term. The evolution of this term with R_f can explain the different behaviour of *G* results compared to *M*.

Fig. 11 shows predicted *FSR* as a function of R_f for 4 test points, the experimental *FSR* are also plotted. The predicted trends with fuel type, λ and with R_f are acceptable especially in the central zone ($R_f > 10mm$ and $R_f < 37mm$). Nothing can be stated about the start of combustion since the experimental results cannot be calculated. Regarding the end of combustion, the prediction does not decrease at the same rate as the experimental data. In this zone the effects of quenching can be proportionally important with respect to the rate of fuel being burned. In predictive models where this correlation is used, it is necessary to complete them with kernel growth and flame quenching models.

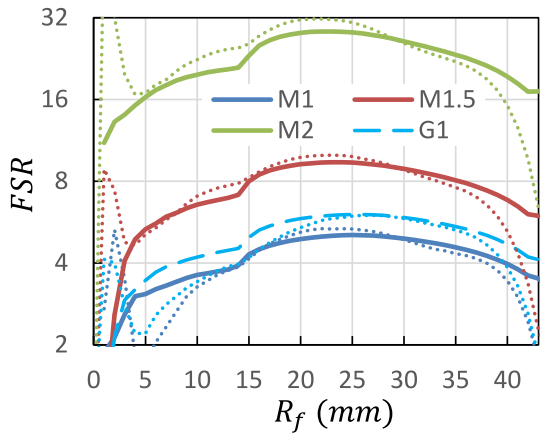

Fig. 11. *FSR* predicted with the correlation as a function of R_f. The experimental values are shown in dotted lines.

6. Conclusions

This investigation provides new knowledge to understand the impact of hydrogen on the combustion characteristics of gasoline/hydrogen fuels in spark ignition engines. A new combustion predictive model is proposed supported by experimental results of an engine running with hydrogen-gasoline mixtures (*M*) in comparison to those of the same engine running with gasoline (*G*). Combustion speed is calculated from the experimental in-cylinder pressure records assuming a spherical flame front centred on the spark plug interacting with the combustion chamber walls. A newly developed geometrical model is developed to estimate the flame front area and radius from the burned products volume underpinned by a 2-zone thermodynamic diagnostic model. The flame front area and the burned mass rate enables to calculate the combustion speed for each crank angle degree and each position (radius) of the flame front as a function of the flame front radius for each test point. The combustion results have been used to develop a model to predict combustion speeds for different fuels including hydrogen.

The predictive model is based on an implicit correlation as a function of the combustion speed, which is solved in a new way using an iterative method underpinned by a fitting methodology based on genetic algorithms. This work demonstrates that the implicit correlation mainly depends on three phenomenological terms. The first and third terms consider the turbulence intensity in the combustion chamber. It is observed that the lower the laminar combustion speed (higher λ), the higher the multiplicative effect of turbulence *FSR*. This means that differences in combustion speeds as λ increases are not the same as would be expected only considering laminar combustion speed. The second term takes into account the influence of the thermo-diffusive properties of the fuel mixture considering the effects of instabilities on combustion speed. This second term shows different trends depending on λ and fuel type, explaining the different behaviour of the G and M results with respect to combustion speeds.

It is concluded that the incorporation of hydrogen to gasoline combustion enables engine operation at higher air excess coefficients (λ) without significantly changing combustion speed and stability. It is demonstrated that hydrogen accelerates the combustion speed mainly at the early stages of the process. The differences on the combustion speed trends between *G* and *M* are explained by the flame front thickness multiplier, which takes into account the effect of combustion instabilities. It is suggested that the combustion regime is thin reactions for all experiments accounting the effect of instabilities. The new knowledge provided in this work and the developed predictive model enable to estimate trends of combustion speeds throughout a variety of combustion chambers, generate new understanding on the combustion process for different fuels and λ providing guidelines for engine developers and researchers, and it can be implemented to complement quasi-dimensional predictive models.

Mendeley data

Giménez, Blanca; Melgar, Andrés; Horrillo, Alfonso; Tinaut, Francisco (2019), "Combustion speed in ICE: thermodynamic model for combustion speed, expansion speed, data base", Mendeley Data, v1. Published: 31 Jul 2019. https://doi.org/10.17632/wskmmkg6rk.1.

Gabana Molina, Pedro; Giménez, Blanca (2024), "Pent-roof Geometric Model", Mendeley Data, V2, https://doi.org/10.17632/fcd8x2n97p.2Credit author statement.

CRediT authorship contribution statement

Pedro Gabana: Software, Methodology, Investigation, Formal analysis. **Blanca Giménez:** Writing – original draft, Resources, Project administration, Conceptualization. **José Martín Herreros:** Writing – review & editing, Supervision, Resources. **Athanasios Tsolakis:** Writing – review & editing, Visualization, Resources, Project administration.

Declaration of competing interest

The authors declare that they have no known competing financial interests or personal relationships that could have appeared to influence the work reported in this paper.

Acknowledgments

Much of the research work carried out has been financed with funds from the Spanish government through the project "Analysis and characterization of dual fuel combustion for the reduction of CO2 emissions in the transport sector" (PID2019-106957RB-C22).

This work would like to also acknowledge the financial support of the EPSRC- EP/W016656/1 "Decarbonised Clean Marine: Green Ammonia Thermal Propulsion (MariNH3)".

P. Gabana has been funded by the 2021 call for pre-doctoral contracts from the University of Valladolid, co-financed by Banco Santander.

The authors would like to thank AVL Advanced Simulation Technologies for allowing the use of the AVL BOOST program in carrying out this work.

The authors would like to thank AUTODESK INVENTOR for allowing the use of its software for the development of this work.

Data availability

Data will be made available on request.

References

[1] Demirbas A. Correlations between Carbon Dioxide Emissions and Carbon Contents of Fuels. Energy Sources Part B 2006;1:421–7. https://doi.org/10.1080/15567240500402628.

[2] Onorati A, Payri R, Vaglieco B, Agarwal A, Bae C, Bruneaux G, et al. The role of hydrogen for future internal combustion engines. Int J Engine Res 2022;23:529–40. https://doi.org/10.1177/14680874221081947.

[3] Salvi BL, Subramanian KA. Sustainable development of road transportation sector using hydrogen energy system. Renew Sustain Energy Rev 2015;51:1132–55. https://doi.org/10.1016/j.rser.2015.07.030.

[4] Kim J, Moon I. The role of hydrogen in the road transportation sector for a sustainable energy system: A case study of Korea. Int J Hydrogen Energy 2008;33:7326–37. https://doi.org/10.1016/j.ijhydene.2008.09.050.

[5] Verhelst S, Wallner T. Hydrogen-fueled internal combustion engines. Prog Energy Combust Sci 2009;35:490–527. https://doi.org/10.1016/j.pecs.2009.08.001.

[6] Dr. P. Kapus, Dr. R. Heindl, M. Weißbäck, Dr. P. Grabner, High Efficiency Hydrogen Internal Combustion Engine – Carbon Free Powertrain for Passenger Car Hybrids and Commercial Vehicles, in: 43rd International Vienna Motor Symposium, Vienna Motor Symposium, Vienna, 2022.

[7] Halder P, Babaie M, Salek F, Haque N, Savage R, Stevanovic S, et al. Advancements in hydrogen production, storage, distribution and refuelling for a sustainable transport sector: Hydrogen fuel cell vehicles. Int J Hydrogen Energy 2024;52:973–1004. https://doi.org/10.1016/j.ijhydene.2023.07.204.
[8] Akal D, Öztuna S, Büyükakın MK. A review of hydrogen usage in internal combustion engines (gasoline-Lpg-diesel) from combustion performance aspect. Int J Hydrogen Energy 2020;45:35257–68. https://doi.org/10.1016/j.ijhydene.2020.02.001.
[9] Ji C, Wang S, Zhang B. Combustion and emissions characteristics of a hybrid hydrogen–gasoline engine under various loads and lean conditions. Int J Hydrogen Energy 2010;35:5714–22. https://doi.org/10.1016/j.ijhydene.2010.03.033.
[10] Ji C, Wang S. Effect of hydrogen addition on the idle performance of a spark ignited gasoline engine at stoichiometric condition. Int J Hydrogen Energy 2009;34:3546–56. https://doi.org/10.1016/j.ijhydene.2009.02.052.
[11] Sadiq Al-Baghdadi M-A-R, Shahad Al-Janabi H-A-K. Improvement of performance and reduction of pollutant emission of a four stroke spark ignition engine fueled with hydrogen–gasoline fuel mixture. Energy Convers Manag 2000;41:77–91. https://doi.org/10.1016/S0196-8904(99)00080-1.
[12] Yavuz M, Brinklow G, Cova Bonillo A, Herreros JM, Wu D, Doustdar O, et al. Alcove Clave, The Suitability of the Three-way Catalyst for Hydrogen Fuelled Engines. Johnson Matthey Technol Rev 2024;68:412–26. https://doi.org/10.1595/205651324X17054113843942.
[13] Zhang B, Wang S, Zhai Y. Estimating the charge burning velocity within a hydrogen-enriched gasoline engine. Int J Hydrogen Energy 2023;48:10264–71. https://doi.org/10.1016/j.ijhydene.2022.12.154.
[14] Giménez B, Melgar A, Horrillo A, Tinaut FV. A correlation for turbulent combustion speed accounting for instabilities and expansion speed in a hydrogen-natural gas spark ignition engine. Combust Flame 2021;223:15–27. https://doi.org/10.1016/j.combustflame.2020.09.026.
[15] Abraham. Savitzky, M.J.E. Golay, Smoothing and Differentiation of Data by Simplified Least Squares Procedures., Anal Chem 36 (1964) 1627–1639. Doi: 10.1021/ac60214a047.
[16] Reyes M, Melgar A, Pérez A, Giménez B. Study of the cycle-to-cycle variations of an internal combustion engine fuelled with natural gas/hydrogen blends from the diagnosis of combustion pressure. Int J Hydrogen Energy 2013;38:15477–87. https://doi.org/10.1016/j.ijhydene.2013.09.071.
[17] Giménez B, Melgar A, Horrillo A, Gabana P. Prediction of the flame kernel growth rate in spark ignition engine fueled with natural gas, hydrogen and mixtures. Fuel 2023;339:126908. https://doi.org/10.1016/j.fuel.2022.126908.
[18] Tahtouh T, Halter F, Mounaïm-Rousselle C. Laminar premixed flame characteristics of hydrogen blended iso-octane–air–nitrogen mixtures. Int J Hydrogen Energy 2011;36:985–91. https://doi.org/10.1016/j.ijhydene.2010.08.148.
[19] Ji C, Liu X, Wang S, Gao B, Yang J. Development and validation of a laminar flame speed correlation for the CFD simulation of hydrogen-enriched gasoline engines. Int J Hydrogen Energy 2013;38:1997–2006. https://doi.org/10.1016/j.ijhydene.2012.11.139.
[20] Gülder ÖL. Laminar burning velocities of methanol, ethanol and isooctane-air mixtures. Symp (Int) Combust 1982;19:275–81. https://doi.org/10.1016/S0082-0784(82)80198-7.
[21] Del Pecchia M, Pessina V, Berni F, d'Adamo A, Fontanesi S. Gasoline-ethanol blend formulation to mimic laminar flame speed and auto-ignition quality in automotive engines. Fuel 2020;264:116741. https://doi.org/10.1016/j.fuel.2019.116741.
[22] Poulos SG, Heywood JB. The Effect of Chamber Geometry on Spark-Ignition Engine Combustion. in 1983. https://doi.org/10.4271/830334.
[23] Bouvet N, Halter F, Chauveau C, Yoon Y. On the effective Lewis number formulations for lean hydrogen/hydrocarbon/air mixtures. Int J Hydrogen Energy 2013;38:5949–60. https://doi.org/10.1016/j.ijhydene.2013.02.098.
[24] M.T. Nguyen, D. Yu, C. Chen, S. (Steven) Shy, General Correlations of Iso-octane Turbulent Burning Velocities Relevant to Spark Ignition Engines, Energies (Basel) 12 (2019) 1848. Doi: 10.3390/en12101848.
[25] Bruce E. Poling, John M. Prausnitz, John P. O'Connell, The Properties of Gases and Liquids, Fifth edition, The McGraw-Hill Companies, Inc, New York Chicago San Francisco Lisbon London Madrid Mexico City Milan New Delhi San Juan Seoul Singapore Sydney Toronto, 2001.
[26] Mathur S, Tondon PK, Saxena SC. Thermal conductivity of binary, ternary and quaternary mixtures of rare gases. Mol Phys 1967;12:569–79. https://doi.org/10.1080/00268976700100731.
[27] P.J., & M.W.G. Linstrom, NIST Chemistry WebBook, NIST Standard Reference Database Number 69, (Gaithersburg, MD: National Institute of Standards and Technology), 2018.
[28] N. Fogla, F. Creta, M. Matalon, The turbulent flame speed for low-to-moderate turbulence intensities: Hydrodynamic theory vs. experiments, Combust Flame 175 (2017) 155–169. Doi: 10.1016/j.combustflame.2016.06.023.
[29] Egolfopoulos FN, Law CK. Chain mechanisms in the overall reaction orders in laminar flame propagation. Combust Flame 1990;80:7–16. https://doi.org/10.1016/0010-2180(90)90049-W.
[30] Ayala FA, Heywood JB. Lean SI Engines: The role of combustion variability in defining lean limits. SAE Technical Paper Series 2007–24-0030 2007. https://doi.org/10.4271/2007-24-0030.
[31] Wang Z, Su X, Wang X, Jia D, Wang D, Li J. Impact of ignition energy on the combustion performance of an SI heavy-duty stoichiometric operation natural gas engine. Fuel 2022;313. https://doi.org/10.1016/j.fuel.2021.122857.
[32] Keum S, Zhu G, Grover R, Zeng W, Rutland C, Kuo T-W. A semi-empirical laminar-to-turbulent flame transition model coupled with G equation for early flame kernel development and combustion in spark-ignition engines. Int J Engine Res 2021;22:479–90. https://doi.org/10.1177/1468087419864748.
[33] Gulder OL. Turbulent premixed flame propagation models for different combustion regimes. Symp (Int) Combust 1990;23:743–50. https://doi.org/10.1016/S0082-0784(06)80325-5.
[34] Peters N. The turbulent burning velocity for large-scale and small-scale turbulence. J Fluid Mech 1999;384:107–32. https://doi.org/10.1017/S0022112098004212.
[35] R. Borghi, Turbulent combustion modelling, Prog Energy Combust Sci 14 (1988) 245–292. Doi: 10.1016/0360-1285(88)90015-9.